


Synthesis, structural characterization and biological evaluation of mononuclear transition metal complexes of zwitterionic dehydroacetic acid *N*-aroylhydrazone ligand

Umashri Kendur¹ | Geeta H. Chimmalagi¹ | Sunil M. Patil¹ | Kalagouda B. Gudasi¹  | Christopher S. Frampton²

¹Department of Studies in Chemistry, Karnatak University, Dharwad 580003 Karnataka, India

²Institute of Materials & Manufacturing, Wolfson Centre for Materials Processing, Brunel University, London, Uxbridge, UK

Correspondence

Kalagouda B. Gudasi, Department of Studies in Chemistry, Karnatak University, Dharwad-580003, Karnataka, India.

Email: kbudasi@gmail.com

Funding information

DST-PURSE Phase II programme; UPE-FAR-I programme

Synthesis and characterization of mononuclear transition metal complexes viz., Co(II), Ni(II), Cu(II) and Zn(II) with a newly designed ligand, (*E*)-2-benzamido-*N'*-(1-(2-hydroxy-6-methyl-4-oxo-4H-pyran-3-yl) ethylidene) benzohydrazide (**H₂L**) are reported. Molecular structures of **H₂L**, Ni(II) and Cu(II) complexes were determined by single-crystal X-ray diffraction studies. The structures were stabilized by various intra/inter-molecular H-bonding, C-H \cdots π and $\pi\cdots\pi$ stacking interactions. **H₂L** exists in zwitterionic form and acts in a monoanionic manner. Ligand/metal ratio was 2:1 for cobalt, nickel and zinc, whereas 1:1 for the copper complex. Co(II), Ni(II) and Zn(II) complexes display distorted octahedral geometry, while the Cu(II) complex shows distorted square pyramidal geometry around the metal ion. Hirshfeld surface analysis and 2D fingerprint plots revealed that **H₂L** and its complexes were supported mainly by H \cdots H, O \cdots H and C \cdots H intermolecular interactions. The synthesized compounds were screened for *in vitro* anti-inflammatory activity by gelatin zymography and the activity was comparable with tetracycline. Their cleavage behavior towards calf thymus DNA has been studied using agarose gel electrophoresis method. **H₂L** and Cu(II) complex were selected by National Cancer Institute (NCI) for *in vitro* single dose testing in the full NCI 60 cell lines panel assay. Finally, molecular docking simulation effectively proves the binding of all the synthesized compounds at cyclooxygenase-2 (COX-2) active sites.

KEYWORDS

(*E*)-2-amino-*N'*-(1-(2-hydroxy-6-methyl-4-oxo-4H-pyran-3-yl)ethylidene) benzohydrazide, anti-inflammatory and anticancer activity, molecular docking, single crystal X-ray diffraction study, transition metal complexes

1 | INTRODUCTION

The profuseness of metal housed compounds in medicine dates from the 16th century,^[1] since then metals or metal-bearing compounds were used in the treatment of

numerous diseases. Most biological molecules (proteins and DNA) are electron-rich, while on the contrary; metal ions are electron-poor, accordingly, there is a general propensity for metal ions to bind to and interact with many essential biological molecules. Metal ions also have a

great affinity for small molecules, like O₂, being essential for life. These considerations have incited much of the past and present interest in devising novel means to use metals or metal-bearing compounds to modulate biological systems.^[2a,b]

Curiosity in metal-based therapy has been revolutionized, as on coordination, not only bioactive ligands may improve their bioactivity profiles, but also inactive ligands might acquire pharmacological properties.^[3a-e] Metal coordination is one of the most efficient approaches to design long-acting or slow-release drugs.^[4] In this regard, hydrazones constitute an important class of biologically active ligand molecules which have fascinated bioinorganic and medicinal chemists due to their versatile coordination behavior, chelating capacity, structural tractability (that can furnish rigidity to the skeletal framework of the prepared metal complexes) and are endowed with various pharmacological properties. Hydrazones in concert with several metals have been widely used as building blocks to produce a large variety of biologically active topologies.^[5a,b] The modularity, candid synthesis, and stability towards hydrolysis of hydrazones can be cited as reasons for their popularity. Functional diversity of azomethine group in hydrazones, characterized by the triatomic structure C-N-N enables its use in numerous fields. Agile analysis of the structure of hydrazone (Figure 1) divulges that it has (i) an imine carbon that has both electrophilic and nucleophilic character, (ii) nucleophilic imine and amino-type nitrogens, (iii) an acidic N-H proton, and (iv) configurational isomerism emanating from the innate nature of C=N bond [6a-c].

Furthermore, Gelatinases shown in a number of physiologic and pathologic conditions play an essential role in inflammation. MMPs (matrix metalloproteinases) are produced by activated inflammatory cells like neutrophils, fibroblasts, macrophages, epithelial cells, and vascular endothelial cells. Overexpression of MMPs in higher grades may be associated with tissue damage in chronic inflammatory diseases such as periodontitis, rheumatoid and osteoarthritis.^[7] Cancer chemotherapy with platinum drugs has been used since the serendipitous discovery of cisplatin's anti-proliferate properties by

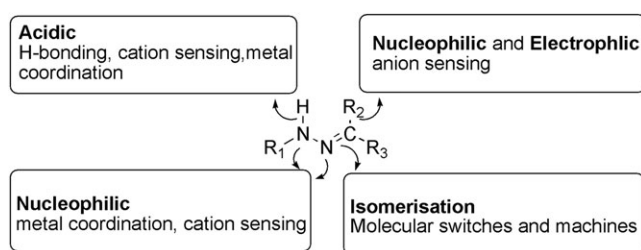


FIGURE 1 The structural and functional diversity of hydrazone scaffold

Rosenberg et al.^[8] Compared to platinum-based drugs, copper-based coordination compounds may act as more potent anticancer agents, with reduced toxicity towards normal cells and may potentially evade the chemoresistance related to platinum-based drugs.^[9]

In line with the above discussion, here we report the synthesis, characterization and crystal structures of transition metal complexes of newly designed tridentate ONO-chelator (**H₂L**). Structural descriptions of **H₂L**, Ni(II) and Cu(II) complexes have been corroborated with calculations of Hirshfeld surfaces which reveal an effect of noncovalent interactions on the properties of the surfaces. The *in vitro* anti-inflammatory potency of all the synthesized compounds by gelatin zymography is comparable to that of tetracycline. **H₂L** and Cu(II) complex were selected by NCI under Development Therapeutic Program (NCI-60 DTP Human Tumor Cell Line Screen) for screening in human cancer cell lines. Further, their cleavage behavior towards calf thymus DNA has been studied using agarose gel electrophoresis method.

2 | EXPERIMENTAL

2.1 | Materials and methods

Dehydroacetic acid received from Alfa-Aesar (Thermo Fisher Scientific, Hyderabad, India) and other reagents from Spectrochem (Spectrochem Pvt. Ltd., Mumbai, India), were used as supplied. Solvents were purified and dried according to standard procedures.^[10] All the metal salts used were in their hydrated form except anhydrous ZnCl₂, i.e., CoCl₂·6H₂O, NiCl₂·6H₂O and CuCl₂·2H₂O. Infrared (IR) spectra of the ligand and its complexes were recorded in KBr discs in the region 4000–400 cm⁻¹ on a Nicolet-6700 FT-IR spectrometer (Thermo Fisher Scientific India Pvt. Ltd., Mumbai, India). The CHN analysis was carried out using a Thermo quest elemental analyzer (Mumbai, India). The ¹H NMR spectra were recorded on AGILENT VNMRS-400 spectrometer (Agilent Technologies India Pvt. Ltd., Bengaluru, India), in DMSO-d₆ solvent. The solution state UV-Vis spectra of all the compounds were recorded in the range of 200–500 nm at 10⁻⁵ mol L⁻¹ in DMF to obtain π – π*, n – π* transitions and in the range of 500–1000 nm at 10⁻³ mol L⁻¹ in DMF to obtain d-d transitions using JASCO V-670 50 UV-Vis spectrophotometer (Antech, Bengaluru, India). Thermal behavior of the complexes was analyzed on a Universal V2.4F TA instrument (TA Instruments, Lukens Drive, New Castle USA), from room temperature to a final temperature of 1000 °C at the heating rate of 10 °C/min. The molar conductivity measurements of 1 mM complex solutions in DMF were carried out on Equiptronics EQ-665 conductivity bridge (Equiptronics, Mumbai, India). The

mass spectrum of the ligand was recorded on an LC-MS Applied Biosystems MDS SCIEX-API 4000 spectrometer (Mangaluru, India). The ESI mass spectral data for all the complexes were obtained using a Waters UPLC-TQD mass spectrometer (Waters Pvt. Ltd. Mumbai, India).

2.2 | Synthesis

2.2.1 | Synthesis of (*E*)-2-benzamido-*N'*-(1-(2-hydroxy-6-methyl-4-oxo-4H-pyran-3-yl)ethylidene) benzohydrazide (H_2L)

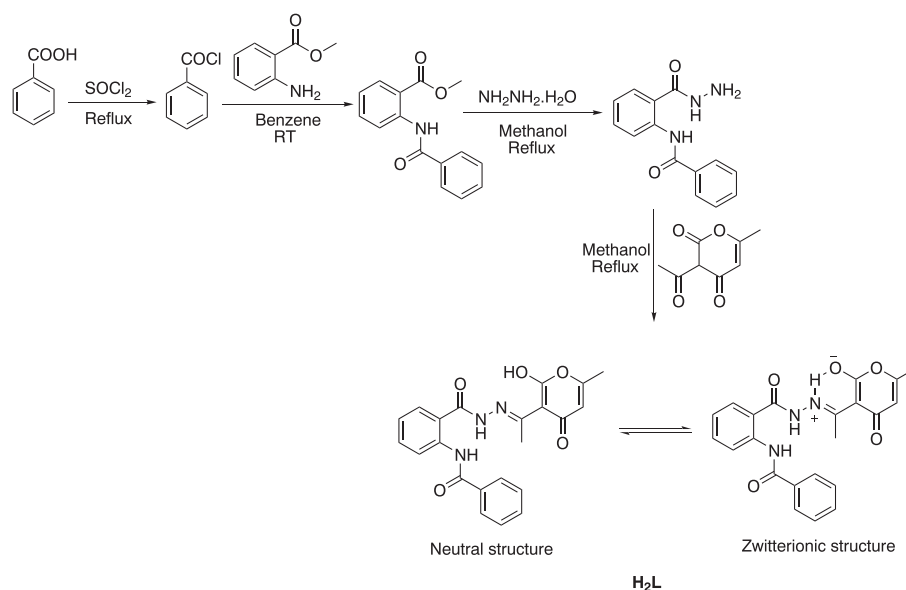
Schematic representation of the synthesis of ligand is given in Scheme 1. First, methyl 2-benzamidobenzoate was obtained from acylation of methyl anthranilate with an acyl chloride by the reported method.^[11] In the next step, methyl 2-benzamidobenzoate (2 g, 7.8 mmol) was refluxed in 20.0 ml of 80% hydrazine hydrate solution, to obtain 2-benzamidobenzohydrazide (1.12 g, Yield: 56%).^[12] Finally, to the magnetically stirred methanolic solution of 2-benzamidobenzohydrazide (2 g, 7.8 mmol), dehydroacetic acid (1.32 g, 7.8 mmol) in methanol was added dropwise. The mixture was refluxed on the water bath for 0.5 h. The progress of the reaction was monitored by TLC. The colorless precipitate formed was filtered and washed with hot methanol. The solid product was dried *in vacuo* for 2 h. Crystals suitable for single X-ray diffraction (SC-XRD) was obtained by slow evaporation of the filtrate.

Yield: 78 %; m.p. 240 °C; Color: colourless. *Anal. Calc.* for $C_{22}H_{19}N_3O_5$: C, 65.18; H, 4.72; N, 10.37. Found for H_2L : C, 65.50; H, 4.97; N, 10.55. FTIR (cm^{-1}): $\nu = 3221$

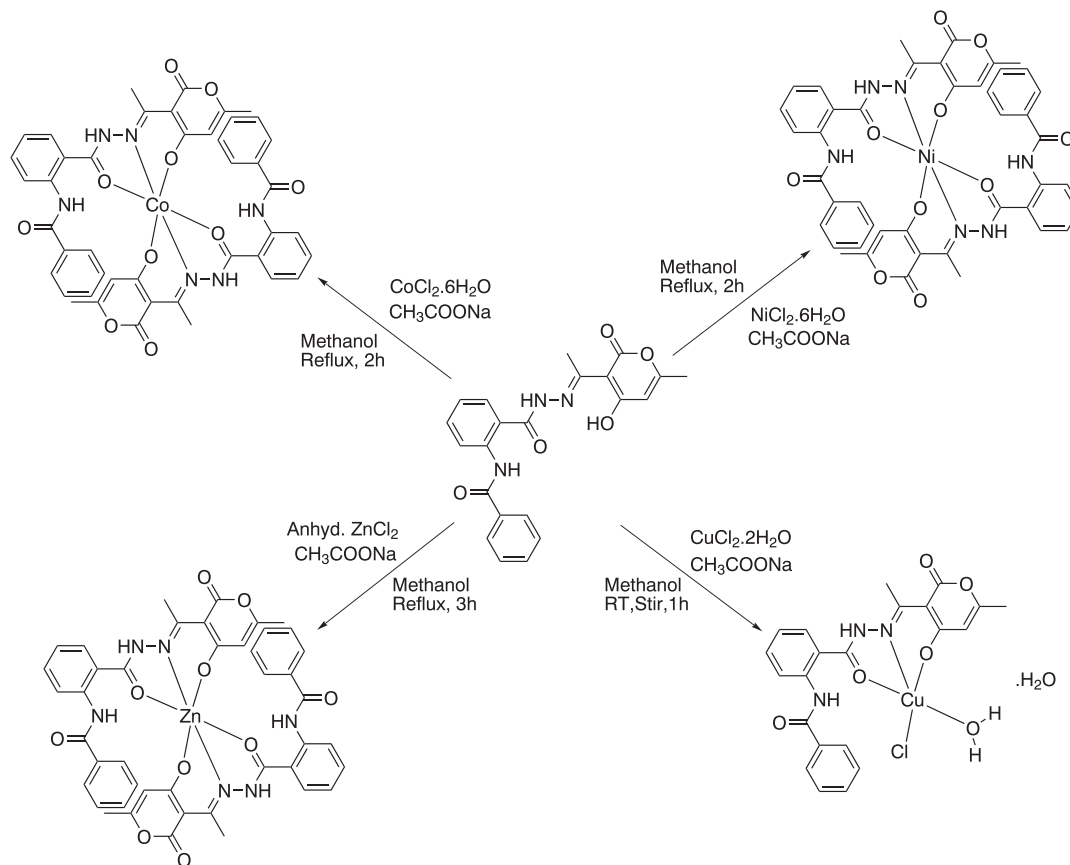
(m, N1-H and N2-H); 1695 (s, pyrone C18=O and lactone C22=O); 1668 (s, amide C14=O); 1651 (s, amide C7=O); 1604 (m, C=N). 1H NMR (DMSO- d_6 , 400 MHz) δ (ppm): 15.89 (s, 1H, O3-H), 11.36 (s, 1H, N1-H), 11.78 (s, 1H, N2-H), 8.33 (d, 1H, ArH, $J=8.4$ Hz), 7.92 (d, 2H, ArH, $J=5.2$ Hz), 7.82 (d, 1H, ArH, $J=8$ Hz), 7.66-7.55 (m, 4H, ArH), 7.29 (t, 1H, ArH, $J=6.8$ Hz), 5.85 (s, 1H, C19-H), 2.61 (s, 3H, C21-H3), 2.11 (s, 3H, C16-H3). LC-MS (m/z): 406 ($[M]^+$). UV/Vis (DMF) λ_{max} , nm ($\log \epsilon$, $L mol^{-1} cm^{-1}$) transitions: 270 (7.66), 304 (7.57) $\pi - \pi^*$, 391 (7.87) $n - \pi^*$.

2.2.2 | Synthesis of metal complexes

Schematic depiction of synthesis of the complexes is given in Scheme 2. Co(II) and Ni(II) complexes were obtained by refluxing the respective hexa hydrated metal chlorides (0.293 g, 1.2 mmol) with the methanolic solution of H_2L (0.500 g, 1.2 mmol) for 2 h. The crystalline product was obtained by evaporating the solvent under reduced pressure. Single crystals were obtained by evaporating the methanolic solution of Ni(II) complex. To the methanolic solution of H_2L (0.500 g, 1.2 mmol), a methanolic solution of $CuCl_2 \cdot 2H_2O$ (0.210 g, 1.2 mmol) was added dropwise and the resulting suspension was stirred for 1 h at room temperature. The green precipitate obtained was filtered off, washed with cold methanol and dried *in vacuo*. Tiny single crystals suitable for SC-XRD were obtained by slow evaporation of the filtrate. Whereas, Zn(II) complex was obtained by refluxing anhydrous $ZnCl_2$ (0.168 g, 1.2 mmol) with the methanolic solution of H_2L (0.500 g, 1.2 mmol) for 3 h. The yellow product was filtered and washed with methanol.



SCHEME 1 Synthetic route for the preparation of H_2L



SCHEME 2 Synthetic route for the preparation of complexes

[Co(HL)₂] (1)

Color: Tyrian purple, Yield: 68%. *Anal. Calc.* for C₄₄H₃₆N₆O₁₀Co: C, 60.90; H, 4.18; Co, 6.79; N, 9.69. Found: C, 60.79; H, 4.29; Co, 6.62; N, 9.58. FTIR (cm⁻¹): ν = 3295 (m, N1-H and N2-H); 1682 (s, lactone C22=O); 1656 (s, amide C7=O); 1614 (s, amide C14=O); 1589 (m, C=N). ESI-MS (positive mode m/z) 868 ([Co(HL)₂-H]⁺). Molar conductivity (Ohm⁻¹ cm² mol⁻¹): 5.2. UV/Vis (DMF) λ_{\max} , nm (log ϵ , L mol⁻¹ cm⁻¹) transitions: 270 (8.27) $\pi - \pi^*$, 380 (7.93) n - π^* , 749 (4.064), 850 (4.22) d-d transitions.

[Ni(HL)₂] (2)

Color: Fern green, Yield: 66%. *Anal. Calc.* for C₄₄H₃₆N₆O₁₀Ni: C, 60.92; H, 4.18; N, 9.69; Ni, 6.77. Found: C, 60.92; H, 4.18; N, 9.69; Ni, 6.77. FTIR (cm⁻¹): ν = 3190 (m, N1-H and N2-H); 1680 (s, lactone C22=O); 1665 (s, amide C7=O); 1620 (s, amide C14=O); 1585 (m, C=N). ESI-MS (positive mode m/z) 868 ([Ni(HL)₂-H]⁺). Molar conductivity (Ohm⁻¹ cm² mol⁻¹): 4.3. UV/Vis (DMF) λ_{\max} , nm (log ϵ , L mol⁻¹ cm⁻¹) transitions: 270 (7.63) $\pi - \pi^*$, 385 (7.65) n - π^* , 560 (5.46), 927 (5.52), 935 (5.53) d-d transitions.

[Cu(HL)Cl(H₂O)].H₂O (3)

Color: Green, Yield: 70%. *Anal. Calc.* for C₂₂H₂₂N₃O₇ClCu: C, 48.98; H, 4.11; Cl, 6.57; Cu, 11.78; N, 7.79. Found: C, 48.75; H, 4.20; Cl, 6.73; Cu, 11.99; N, 7.65. FTIR (cm⁻¹): ν = 3377 (m, N1-H and N2-H); 1695 (s, lactone C22=O); 1674 (s, pyrone C18=O); 1645 (s, amide C7=O); 1618 (s, amide C14=O); 1592 (m, C=N). ESI-MS (positive mode m/z) 545 ([Cu(HL)Cl(H₂O)]+Na]⁺), 522 ([Cu(HL)Cl(H₂O)]⁺), 467 [Cu(HL)]⁺. Molar conductivity (Ohm⁻¹ cm² mol⁻¹): 32. UV/Vis (DMF) λ_{\max} , nm (log ϵ , L mol⁻¹ cm⁻¹) transitions: 270 (7.88) $\pi - \pi^*$, 371 (7.87) n - π^* , 659 (5.17) d-d transitions.

[Zn(HL)₂] (4)

Color: Yellow, Yield: 60%. *Anal. Calc.* for C₄₄H₃₆N₆O₁₀Zn: C, 60.45; H, 4.15; N, 9.61; Zn, 7.48. Found: C, 60.65; H, 4.02; N, 9.53; Zn, 7.39. FTIR (cm⁻¹): ν = 3323 (m, N1-H and N2-H); 1677 (s, lactone C22=O); 1656 (s, amide C7=O); 1627 (s, amide C14=O); 1598 (m, C=N). ESI-MS (positive mode m/z) 871 ([Zn(HL)₂-H]⁺). ¹H NMR (DMSO-d₆, 400 MHz) δ (ppm): 11.80 (s, 1H, N1-H), 12.65 (s, 1H, N2-H), 8.40 (d, 1H, ArH, J=8.4 Hz), 7.91 (d, 2H,

ArH, $J=5.2$ Hz), 7.61-7.53 (m, 5H, ArH), 7.19 (t, 1H, ArH, $J=6.8$ Hz), 5.76 (s, 1H, C19-H), 2.59 (s, 3H, C21-H3), 2.06 (s, 3H, C16-H3). Molar conductivity ($\text{Ohm}^{-1} \text{cm}^2 \text{mol}^{-1}$): 7.6. UV/Vis (DMF) λ_{max} , nm ($\log \epsilon$, $\text{L mol}^{-1} \text{cm}^{-1}$) transitions: 269 (8.08) $\pi - \pi^*$, 379 (8.19) $n - \pi^*$.

2.3 | X-ray crystallography

Selected crystals of **H₂L**, **2** and **3** were mounted on the tip of a 200 μm Mitagen loop with perfluorinated oil and cooled rapidly to 100 K in a stream of cold nitrogen. Data were collected on an Oxford Diffraction, (Agilent Technologies, Santa Clara, USA), SuperNova X-ray diffractometer equipped with an Oxford Cryosystems Cobra Low-temperature device using Cu $K\alpha$ radiation ($\lambda = 154.178$ pm) from a SuperNova Cu X-ray micro source and focusing mirror optics. The structures were solved by direct methods and refined against F^2 by full-matrix least-squares using the program SHELXL-2014/6.^[13]

2.4 | Hirshfeld surface analysis

Hirshfeld surfaces (HSs) and 2D fingerprint plots (FPs) were generated using Crystal Explorer 3.1^[14] based on results of SC-XRD studies. The function d_{norm} is a ratio encompassing the distances of any surface point to the nearest interior (d_i) and exterior (d_e) atom and the van der Waals radii of the atoms.^[15, 16a] The negative value of d_{norm} indicates the sum of d_i and d_e is shorter than the sum of the relevant van der Waals radii, which is considered to be the closest contact and is visualized as red color in the HSs. The white color denotes intermolecular distances close to van der Waals contacts with d_{norm} equal to zero whereas contacts longer than the sum of van der Waals radii with positive d_{norm} values are colored with blue.^[16b] A plot of d_i versus d_e is a 2D fingerprint plot which recognizes the existence of different types of intermolecular interactions.

2.5 | Pharmacology results

2.5.1 | *In vitro* Anti-inflammatory screening

Detection of MMP-2 and MMP-9 by gelatin zymography through gel electrophoresis

In vitro anti-inflammatory activity was carried out as described by Shastri *et al.*^[17] 10 mg of all synthesized compounds were dissolved in 1 ml of DMSO, hence, each μL contains 10 μg of the compound. 50 μL of MMP extract and 50 μL of synthesized compounds were

blended independently and afterwards brooded for 15-30 min. Non reducing buffer in equal volume was added, blended and 20 μL was filled in each well employing gel loading pipette tips and 10 μL molecular weight marker was filled in last well. 0.9% normal saline with 50 μL of the tissue sample is used as the control. Initially, the gel electrophoresis apparatus was run at about 100 V until the bromophenol blue reached the bottom of the plates. After electrophoresis, the equipment was disassembled, the gel was gently detached and the equipment was washed with zymogram renaturing buffer and let the proteins to denature. Later, the gel was incubated in zymogram incubation buffer at 37 °C overnight and smeared with Coomassie blue R250 for one hour. Presence of gelatinases appeared as white bands, the upper bands are gelatinase-B (MMP-9) while the lower bands are gelatinase-A (MMP-2). Using gel documentation system, the percentage of inhibition was assigned.

2.5.2 | NCI-60 Human Cancer Cell Line Screening methodology

Compounds **H₂L** and **3** were screened against a panel of 60 human cancer cell lines at NCI. Screening is a two-step process, first a single concentration is tested against all 60 cell lines at a single dose of 10^{-5} M. If the results obtained meet selection standards, then the compound is tested once more against all 60 cell lines in 5 x 10 fold dilutions with the top dose of 10^{-4} M. Compounds consented for NCI60 testing are prepared for both 1-dose and 5-dose testing at the same time. The One-dose data were reported as a mean graph of the percent growth of treated cells. The number reported for the One-dose assay is growth relative to the no-drug control, and relative to the time zero number of cells. This allows the detection of both growth inhibition (values between 0 and 100) and lethality (values less than 0). A value of 0 means no net growth over the course of the experiment and a value of -100 means all cells are dead.^[18a-c]

2.5.3 | DNA cleavage studies

Agarose gel electrophoresis

Cleavage results were analyzed by agarose gel electrophoresis method.^[19] Nutrient broth media was used (NaCl 10, Peptone 10 and yeast extract 5 g L^{-1}). The degree to which the ligand and its complexes can function as DNA cleavage agents were examined using calf-thymus DNA as a target. 250 mg of agarose was dissolved in 25 ml of tris- acetate-EDTA (TAE) buffer (4.84 g tris base, pH 8.0; 0.5 M EDTA L^{-1}) by boiling,

when the gel reaches ~55 °C, it was poured into gel cassette fitted with a comb and left it to solidify. Then comb was removed carefully and the gel was placed in the electrophoresis chamber deluged with TAE buffer. 20 μL of DNA sample was filled (mixed with bromophenol blue dye at 1:1 ratio) cautiously into the wells, along with standard DNA marker with a constant 50 V of electricity for 45 min. Finally, the gel was detached and cautiously stained with ethidium bromide solution (10 μL^{-1}) for 15 min and the bands were observed under UV transilluminator.

2.5.4 | Docking studies

To identify the potential structural features for anti-inflammatory activity and interaction at the active site of a protein, molecular docking studies have been performed. The crystal structure of celecoxib bound COX-2 (PDB ID: 3LN1) derived from RSC PDB website (<http://www.rcsb.org/pdb>).^[20] AutoDock Vina^[21] together with the AutoDock Tools was employed to perform blind docking calculations of ligand and complexes binding to COX-2.

TABLE 1 Crystal data and structure refinement details of **H₂L**, **2** and **3**

Empirical formula	C ₂₂ H ₁₉ N ₃ O ₅	C ₄₄ H ₄₄ N ₆ NiO ₁₄	C ₂₂ H ₂₂ ClCuN ₃ O ₇
Formula weight	405.40	939.56	539.41
Temperature/K	100(1)	100(1)	100(1)
Wavelength/Å	1.54184	1.54178	1.54178
Crystal system	monoclinic	triclinic	monoclinic
Space group	P2 ₁ /n	P-1	P2 ₁ /n
a/Å	9.68635(13)	8.9604(4)	14.4806(7)
b/Å	10.97725(14)	14.8953(5)	16.9721(7)
c/Å	18.1862(2)	17.0710(4)	19.4500(8)
α /°	90	101.758(3)	90
β /°	93.0043(12)	100.292(3)	106.220(5)
γ /°	90	100.872(3)	90
Volume/Å ³	1931.08(4)	2134.01(13)	4589.9(4)
Z	4	2	8
ρ_{calc} g/cm ³	1.394	1.462	1.561
μ /mm ⁻¹	0.835	1.316	2.850
F(000)	848.0	980.0	2216.0
Crystal size/mm ³	0.413 × 0.256 × 0.153	0.313 × 0.094 × 0.058	0.155 × 0.121 × 0.101
2 θ range for data collection/°	9.414 to 148.976	5.428 to 148.976	6.782 to 149.006
Index ranges	-11 ≤ h ≤ 12, -13 ≤ k ≤ 11, -22 ≤ l ≤ 22	-10 ≤ h ≤ 11, -18 ≤ k ≤ 18, -21 ≤ l ≤ 20	-18 ≤ h ≤ 16, -21 ≤ k ≤ 18, -18 ≤ l ≤ 24
Reflections collected	8117	17303	21656
Independent reflections	3942 [R _{int} = 0.0149, R _{sigma} = 0.0186]	8712 [R _{int} = 0.0199, R _{sigma} = 0.0290]	9358 [R _{int} = 0.0192, R _{sigma} = 0.0237]
Data/restraints/parameters	3942/0/285	8712/0/614	9358/0/633
Goodness-of-fit on F ²	1.031	1.024	1.006
R ₁ ,wR ₂ ^{a,b} [I > 2 σ (I)]	R1 = 0.0347, wR2 = 0.0883	R1 = 0.0495, wR2 = 0.1370	R1 = 0.0350, wR2 = 0.0973
R ₁ ,wR ₂ ^{a,b} [all data]	R ₁ = 0.0367, wR ₂ = 0.0900	R ₁ = 0.0535, wR ₂ = 0.1416	R ₁ = 0.0391, wR ₂ = 0.1004
Largest diff. in peak and hole / e Å ⁻³	0.22/-0.28	0.95/-0.78	0.44/-0.81

^aR₁ = $\|F_o\| - \|F_c\|/\|F_o\|$.

^bR₂ = $[\sum w(|F_o|^2 - |F_c|^2)|^2 / \sum w |F_o|^2]^{1/2}$.

The coordinates of the complexes were taken from the crystal structures as a CIF file and converted to the PDB format using Mercury software. For all the other structures (where X-ray structures are not available) the geometry was optimized with ORCA (Quantum Chemistry Program) package.^[22] All calculations were performed using the hybrid functional BP in combination with Ahlrichs split-valence double- ξ basis set def2-SVP^[23] for all the atoms. The output of the calculations was visualized using molecular visualizer tool Avogadro 1.1.1.^[24] The receptor and the 'ligand' (ligand and its complexes) input files were prepared using UCCF Chimera 1.11rc^[25] and Autodock tools. In the docking analysis, the binding site was assigned to include the entire protein, which was enclosed in a box with a number of grid points in $x \times y \times z$ directions, $48 \times 33 \times 25$ and a grid spacing of 0.375 Å. After generation of the grid map, AutoDock Vina was run by using parameters as follows: GA population size, 150; maximum number of energy evaluations, 2,500,000; numbers of generations, 27,000. A total of 50

runs were carried out. A maximum of 50 conformers was considered for each molecule, and the root-mean-square cluster tolerance was set to 2.0 Å in each run. For each docking cases, lowest energy docked conformation, according to the AutoDock Vina scoring function was selected as the binding mode. Visualization of the docked pose has been done by using Python Molecule Viewer^[26] and Discovery Studio Visualizer.

3 | RESULTS AND DISCUSSION

3.1 | Crystallographic study

Single crystals of **H₂L**, **2** and **3** suitable for SC-XRD studies were grown by slow evaporation technique. Summaries of the crystallographic data, selected bond angles and bond lengths, and hydrogen bond dimensions of **H₂L**, **2** and **3** are compiled in Tables 1–4, respectively. ORTEP representations of the same showing 50% displacement ellipsoids along with the numbering scheme are displayed in

TABLE 2 Selected bond angles of **H₂L**, **2** and **3**

H₂L		2		3	
N2-C14-C13	115.1(9)	N2A-C14A-C13A	115.6(17)	N2A-C14A-C13A	116.5(16)
		C36A-N5A-N6A	116.4(18)	N2B-C14B-C13B	116.6(17)
C14-N2-N3	114.8(9)	C14A-N2A-N3A	116.4(16)	C14A-N2A-N3A	116.0(15)
		N5A-C36A-C35A	117.8(18)	C14B-N2B-N3B	115.3(15)
C15-N3-N2	121.8(9)	C15A-N3A-N2A	118.1(16)	C15A-N3A-N2A	117.7(15)
		C37A-N6A-N5A	118.9(18)	C15B-N3B-N2B	117.6(15)
N3-C15-C17	115.4(9)	N3A-C15A-C17A	119.2(18)	N3A-C15A-C17A	118.3(17)
		N6A-C37A-C39A	119.1(19)	N3B-C15B-C17B	118.7(16)
O2-C14-N2	121.1(9)	O2A-C14A-N2A	121.2(18)	O2A-C14A-N2A	120.4(17)
		O7A-C36A-C35A	121.1(18)	O2B-C14B-N2B	120.6(17)
O3-C18-C17	122.8(10)	O3A-C18A-C17A	125.9(2)	O3A-C18A-C17A	126.1(18)
		O8A-C40A-C39A	126.8(2)	O3B-C18B-C17B	126.1(17)
C18-C17-C15	119.6(9)	C18A-C17A-C15A	124.8(2)	C18A-C17A-C15A	123.6(17)
		C40A-C39A-C37A	123.9(19)	C18B-C17B-C15B	123.4(16)
		O3A-Cu1A-N3A	89.78(6)	O8A-Ni1A-O3A	95.61(7)
		O3B-Cu1B-N3B	89.45(6)	O3A-Ni1A-N6A	96.81(7)
		N3A-Cu1A-O2A	81.37(6)	O3A-Ni1A-N3A	89.87(7)
		N3B-Cu1B-O2B	80.81(6)	O3A-Ni1A-O7A	90.85(7)
		O2A-Cu1A-Cl1A	93.98(4)	O8A-Ni1A-O2A	88.03(7)
		O2B-Cu1B-Cl1B	94.85(4)	O8A-Ni1A-O3A	95.61(7)
		Cl1A-Cu1A-O6A	94.26(4)	N6A-Ni1A-O2A	93.38(7)
		Cl1B-Cu1B-O6B	90.65(4)	N3A-Ni1A-O2A	79.50(6)
		O3A-Cu1A-O6A	98.49(6)	O7A-Ni1A-O2A	87.33(6)
		O3B-Cu1B-O6B	101.2(6)		

TABLE 3 Selected bond distances of **H₂L**, **2** and **3**

H₂L		2		3	
O3-C18	1.273(13)	O3A-C18A	1.275(3)	O3A-C18A	1.280(2)
		O8A-C40A	1.267(3)	O3B-C18B	1.280(2)
N3-C15	1.309(14)	N3A-C15A	1.298(3)	N3A-C15A	1.309(2)
		N6A-C37A	1.301(3)	N3B-C15B	1.311(2)
N2-N3	1.387(12)	N2A-N3A	1.401(2)	N2A-N3A	1.390(2)
		N5A-N6A	1.397(3)	N2B-N3B	1.393(2)
N2-C14	1.362(14)	N2A-C14A	1.344(3)	N2A-C14A	1.330(2)
		N5A-C36A	1.343(3)	N2B-C14B	1.335(2)
O2-C14	1.232(13)	O2A-C14A	1.253(2)	O2A-C14A	1.265(2)
		O7A-C36A	1.256(3)	O2B-C14B	1.260(2)
		Ni1A-O8A	1.969(16)	Cu1A-O3A	1.920(14)
		Ni1A-O3A	1.989(17)	Cu1B-O3B	1.915(13)
		Ni1A-N6A	2.007(17)	Cu1A-N3A	1.960(16)
		Ni1A-N3A	2.009(16)	Cu1B-N3B	1.971(16)
		Ni1A-O7A	2.072(16)	Cu1A-O2A	2.006(13)
		Ni1A-O2A	2.107(15)	Cu1B-O2B	2.007(13)
				Cu1A-Cl1A	2.231(5)
				Cu1B-Cl1B	2.247(5)
				Cu1A-O6A	2.259(15)
				Cu1B-O6B	2.259(15)

TABLE 4 Hydrogen bonds (Å, °) for **H₂L**, **2** and **3**

D-H...A^a interactions	d(D-H)/Å	d(H...A)/Å	d(D...A)/Å	D-H...A/°
H₂L				
N1-H1B...O2	0.900(16)	1.890(16)	2.653(12)	141.3(14)
N2-H2B...O1 ^{#1}	0.914(16)	1.875(16)	2.784(12)	172.8(14)
N3-H3B...O3	1.03(2)	1.53(2)	2.448(12)	145.1(18)
2				
N1A-H1B...O2A	0.82(3)	2.10(3)	2.783(2)	140(2)
N2A-H2B...O1A ^{#2}	0.85(3)	1.97(3)	2.815(2)	173(3)
N4A-H4B...O7A	0.81(3)	2.08(3)	2.719(2)	136(3)
N5A-H5B...O6A ^{#3}	0.84(3)	2.08(3)	2.909(2)	169(3)
3				
O6A-H6AA...O1C	0.89	2.09	2.923(2)	156.3
N1A-H1A...O2A	0.88	2.05	2.748(2)	135.5
N2A-H2A...O1A ^{#4}	0.88	2.05	2.828(2)	146.6
O6A-H6AB...O4B	0.69(3)	2.62(3)	3.171(2)	138(3)
O6A-H6AB...O5B	0.69(3)	2.15(3)	2.828(2)	168(3)
O6B-H6BA...O2C	0.89	2.06	2.930(3)	166.5
N1B-H1B...O2B	0.88	2.07	2.729(2)	131.4

(Continues)

TABLE 4 (Continued)

D-H...A ^a interactions	d(D-H)/Å	d(H...A)/Å	d(D...A)/Å	D-H...A/°
N2B-H2B...O1B ^{#5}	0.88	2.08	2.920(2)	158.7
O6B-H6BB...O5A	0.68(3)	2.05(3)	2.724(2)	171(4)
O1C-H1CA...Cl1A	0.87	2.37	3.219(18)	164.4
O1C-H1CB...Cl1A ^{#6}	0.87	2.92	3.728(2)	155.8
O2C-H2CA...Cl1B	0.87	2.38	3.138(3)	145.8
O2C-H2CB...Cl1B ^{#7}	0.87	2.74	3.582(3)	162.2

D:donor; A:acceptor

^aSymmetry codes:^{#1}1-x,1-y,-z,^{#2}2-x,1-y,2-z;^{#3}1-x,-y,1-z,^{#4}1-x,1-y,2-z;^{#5}1-x,1-y,1-z;^{#6}1-x,2-y,2-z;^{#7}1-x,2-y,1-z.

Figures 2–4. Molecular packing diagrams and molecular planes of **H₂L**, **2** and **3** are presented in the Figures 5–7, respectively.

3.1.1 | Crystal structure of H₂L

H₂L crystallizes as colorless crystals were determined at 100 K is shown to be monoclinic with space group *P*2₁/*n* and *R*₁ is found to be 3.43%. The asymmetric unit of **H₂L** consists of one molecule. Azomethine and ^νC=O (mean of O2-C14-N2-N3-C15) form a dihedral angle of

21.30° with one phenyl ring (mean of C8–C13), 55.12° with another phenyl ring (mean of C1–C6) and 13.08° with DHA ring (mean C17–C18–C19–C20–O4–C22), respectively. Further, the azomethine ^νC=N bond distance (1.309(14) Å) agrees well with the values for double bond character confirming the formation of imine bond. The torsion angle of -9.21(14)° exhibited by N3–N2–C14–O2, -2.72(16)° by C15–C17–C18–O3 and 7.28(18)° by C15–C17–C22–O5 indicate that N3,O2; C15,O3 and C15, O5 are *cis* to each other, respectively, while the torsion angle of 162.65 (9)° exhibited by C14–N2–N3–C15 and

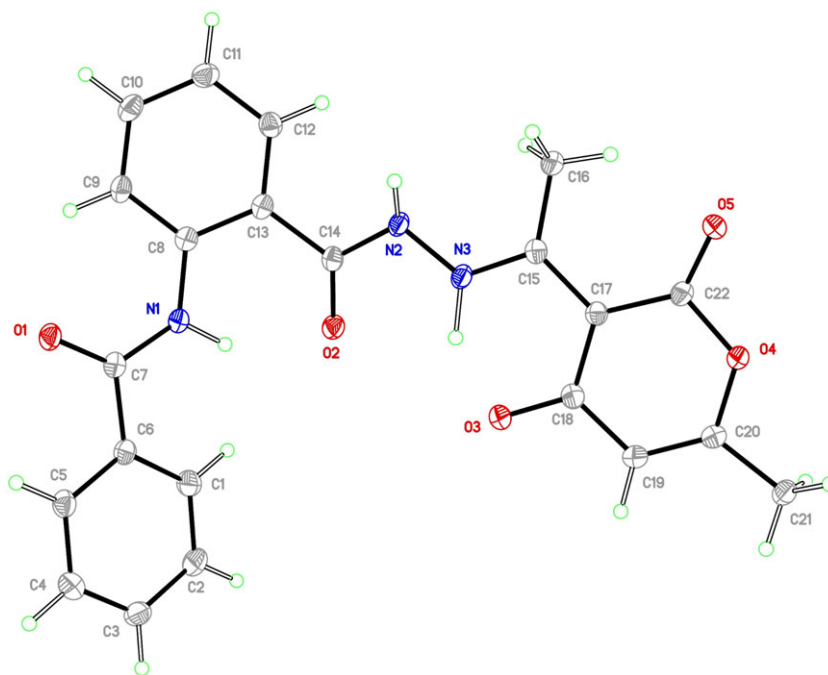


FIGURE 2 ORTEP projection of **H₂L** showing 50% probability ellipsoids

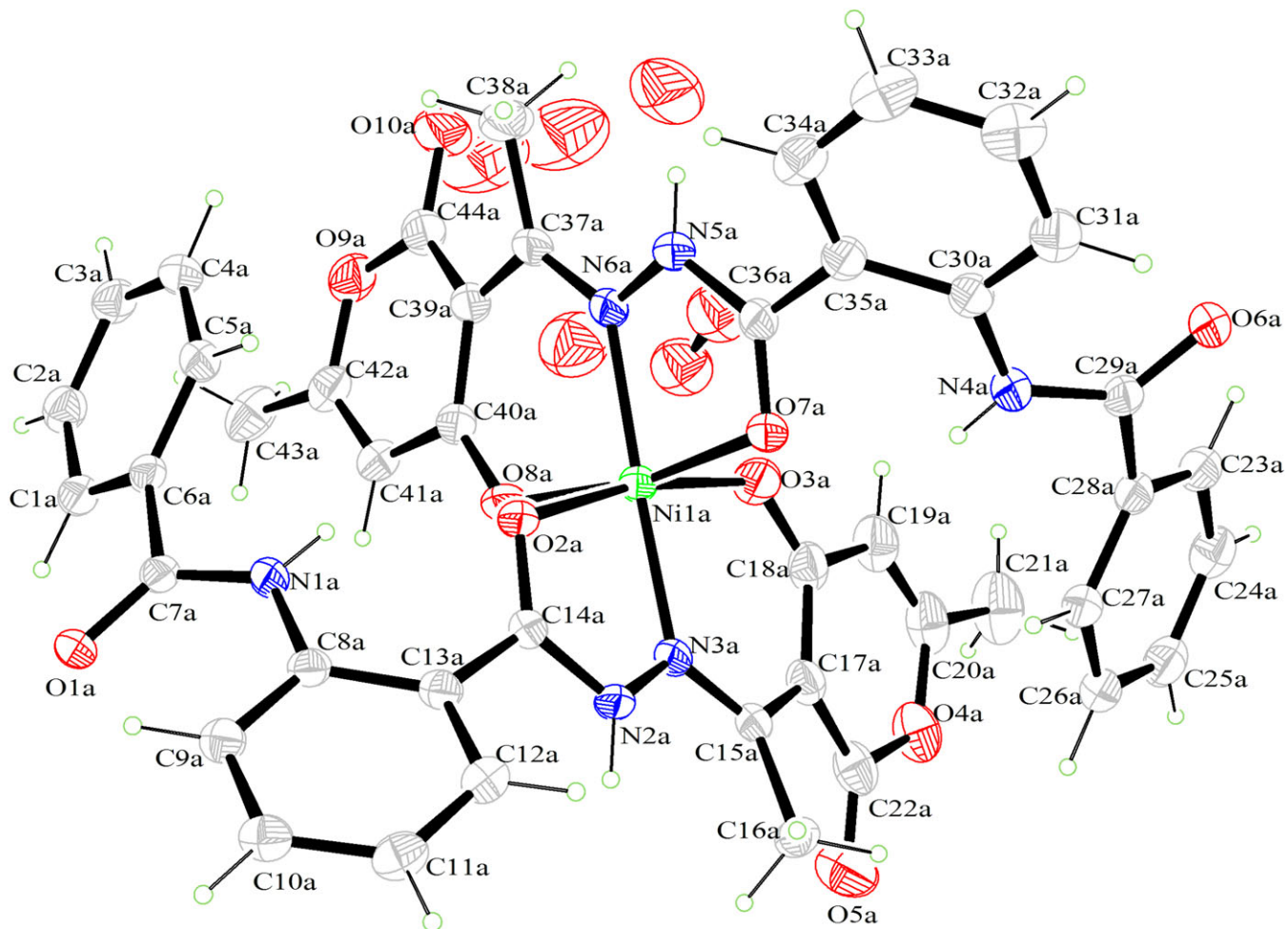


FIGURE 3 ORTEP projection of 2 showing 50% probability ellipsoids

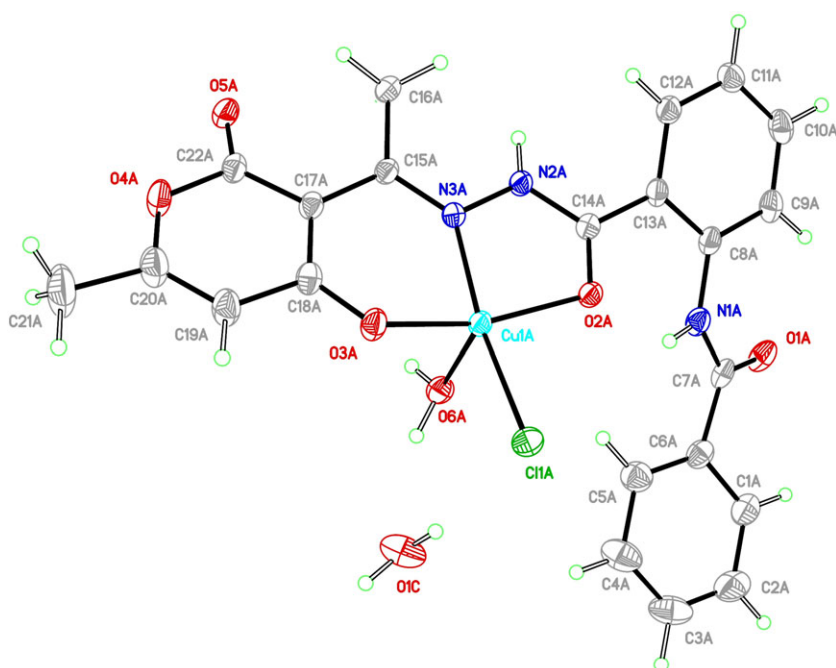


FIGURE 4 ORTEP projection of 3 showing 50% probability ellipsoids

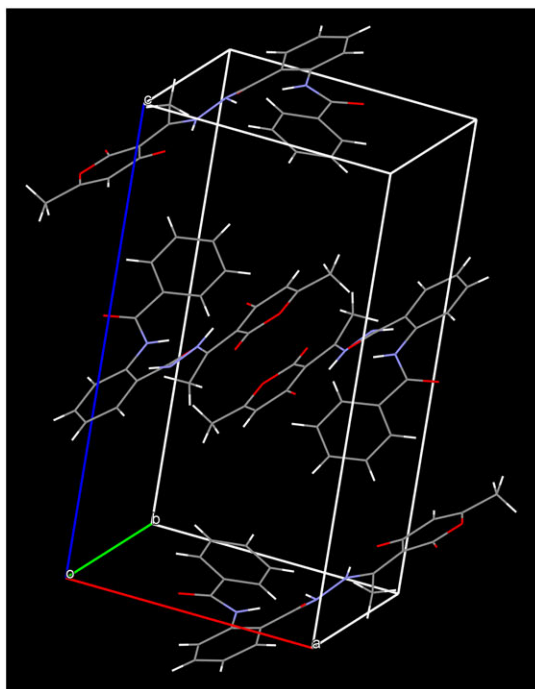


FIGURE 5 Molecular packing and molecular planes in H_2L

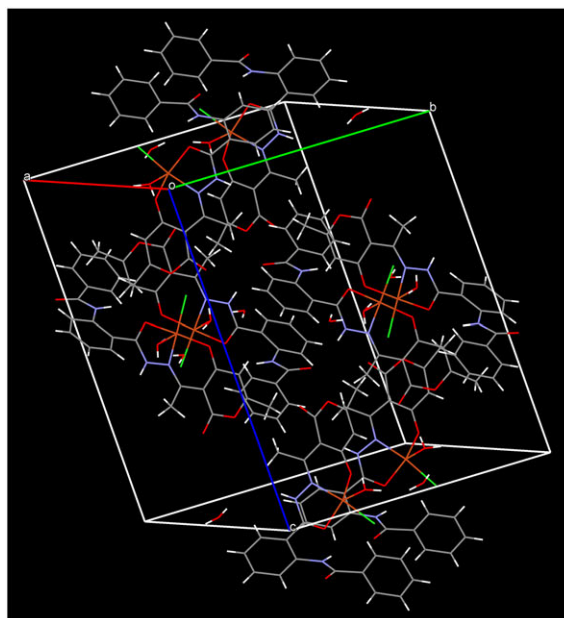


FIGURE 6 Molecular packing and molecular planes in **2**

$-177.94 (9)^\circ$ by $N2-N3-C15-C17$ indicate that $C14$, $C15$ and $N2$, $C17$ are *trans* to each other, respectively. The keto form of the free ligand is evident from the single bond nature of $C14-N2$ bond and the double bond character of $C14-O2$ bond. The ligand is found to exist in zwitterionic form and formally a neutral species as evident by the presence of hydrogen atom ($H3B$) on $N3$ rather than

$O3$, where there exists a single bond character for $C18-O3$ bond.^[27] Two intramolecular hydrogen bonds, involving $N1-H1B$ with $O2$ and $N3-H3B$ with $O3$ are observed. In addition, the molecule is also stabilized *via* one intermolecular hydrogen bond: $N2-H2B \cdots O1$ (1- x , 1- y , $-z$). Dimensions for hydrogen bonds are given in Table 4 and shown in Figure S1.

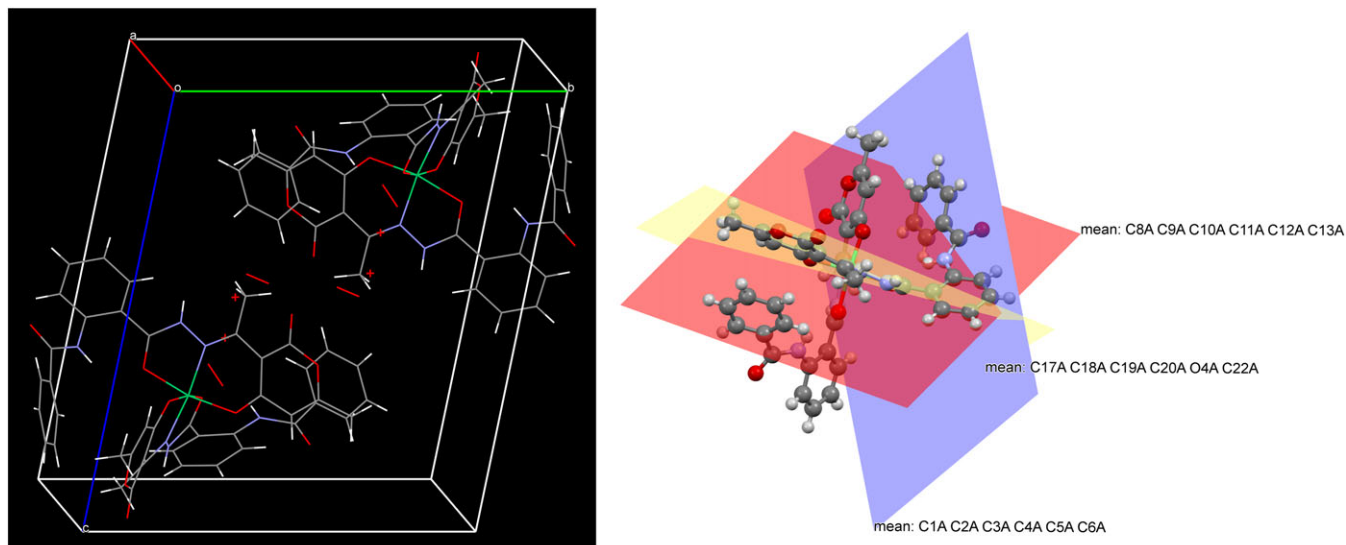


FIGURE 7 Molecular packing and molecular planes in **3**

3.1.2 | Crystal structures of **2** and **3**

Complex **2** crystallizes as fern green colored crystals belong to Triclinic crystal system having space group P-1, while **3** crystallizes as green colored crystals belong to Monoclinic crystal system, in space group P2₁/n. Identical atom-labelling schemes have been adopted for both the structures for easy comparison of their relevant metrical parameters.

Complex **2** was determined at 100 K and R₁ is found to be 4.95%. The asymmetric unit of **2** consists of one molecule. Complex **2** comprise of a neutral unit composed of a central Ni(II) ion in a distorted octahedral environment surrounded by two tridentate mononegative hydrazone (**H₂L**) bound in a *mer* fashion through amide carbonyl oxygen (O2), azomethine nitrogen (N3) and pyrone carbonyl oxygen (O3H) *via* deprotonation. There is some disordered solvent present in the lattice, (currently modelled as oxygen for water). This solvent is present in voids of the lattice. Approximately 12.5% of the structure volume is void space [Figure S4]. The bonds Ni1A–O2A (2.107 Å), Ni1A–N3A (2.009 Å), Ni1A–O3A (1.989 Å), Ni1A–O7A (2.072 Å), Ni1A–N6A (2.007 Å) and Ni1A–O8A (1.970 Å), forming pair of five-membered CN₂ONi and a pair of six-membered C₃NONi chelate rings with bite angles of 79.50°, 79.97°, 89.87° and 89.84°, respectively, represents distortion from an ideal octahedral geometry.^[28] The bond lengths in **2** are: O3A–C18A = 1.275(3), N3A–C15A = 1.298(3) and O2A–C14A = 1.253(2) Å, which are longer or shorter than those of the corresponding distances in the free ligand, O3–C18 = 1.273(13), N3–C15 = 1.309(14) and O2–C14 = 1.232(13) Å is due to the bonding of the Ni(II) center with

the ligand. The crystal is stabilized by two intramolecular N1A–H1B...O2A, N4A–H4B...O7A and two intermolecular N2A–H2B...O1A (2-x,1-y,2-z), N5A–H5B...O6A (1-x,-y,1-z) hydrogen-bonding (Figure S1). In addition, the complex molecule is stabilized by a number of intra/inter-molecular C–H...π and π...π stacking interactions (Figure S2).

Single-crystal X-ray structure of **3** was determined at 100 K and R₁ is found to be 3.50%. The asymmetric unit of **3** consists of two molecules namely A and B. These two molecules A and B differ marginally from one another in their bond distances and bond angles. Such crystallographically independent and chemically similar molecules are known as bond stretch isomers.^[29] The structure of **3** is a neutral molecule with one lattice held water molecule. The ligand is coordinated to the central Cu(II) ion in an ONO tridentate fashion through an amide carbonyl oxygen (O2), azomethine nitrogen (N3) and pyrone carbonyl oxygen (O3H) *via* deprotonation. In addition, contains one coordinated chloride and one coordinated water molecule. This way, **3** adopts a five-coordinate geometry. However, a five-coordinate complex can either adopt a square-pyramidal or trigonal bipyramidal (TBP) geometry. Addison *et al.*^[30] have devised a criterion for assigning a definitive structure to five-coordinate complexes. The formula, $\tau = (\beta - \alpha)/60$ where, α and β are the two biggest angles, defines the index of trigonality (distortion from trigonal-bipyramidal or square-pyramidal geometry) and has been successfully used to distinguish between a square-pyramidal and a TBP configuration. When τ is 0, the structure is square-pyramidal but when τ is 1, the structure is TBP. Using this criterion, the τ value of **3** came to be 0.179 indicating that the

Cu(II) adopts a structure closer to square-pyramidal. The ONO donor sites of the tridentate ligand coordinate the Cu(II) center forming one five-membered CN₂OCu and other six-membered C₃NOCu chelate rings with bite angles of 80.81° and 89.45°, respectively, represents slight distortion from an ideal square pyramidal geometry. The average bond lengths in the complex are: O3–C18 = 1.280(2), N3–C15 = 1.310(2) and O2–C14 = 1.263(2) Å, which are longer or shorter than those of the corresponding distances in the ligand, suggesting considerable delocalization of the charge on the chelate rings.^[31] The crystal is stabilized by three intramolecular O6–H6···O1, N1–H1···O2, O1–H1···Cl1 and two intermolecular N2–H2···O1 (1-x,1-y,2-z), O2–H2···Cl1 (1-x,2-y,1-z) hydrogen-bonding [Figure S1]. In addition, the complex molecule is stabilized by a number of intra /inter-molecular C–H···π and π···π stacking interactions (Figure S3).

There are also two other potential donor sites in the coordinated hydrazone ligand viz., oxygen of amide carbonyl C7=O1 and oxygen of lactone carbonyl C22=O5 which are not coordinated in both **2** and **3** due to their non-planarity with the three donor sites (Figure 5–7). In both the complexes metal-oxygen (M–O) bond lengths are: M–O_{3pyrone} < M–O_{2amido} probably due to the order of O→M π-bonding.^[32] The CIF files have been deposited with CCDC No. 1579095 (**H₂L**), 1579100 (**2**) and 1579096 (**3**).

3.2 | Hirshfeld surface analysis

Hirshfeld surface analysis is rapidly gaining importance as a useful technique in understanding the nature of intermolecular interactions within a crystal structure using a fingerprint plot. This allows easy identification of characteristic interactions throughout the structure. In order to measure various intermolecular interactions, HSs and their associated FPs were generated using Crystal Explorer 3.1. Even weak interactions, such as C–H···π, C···H, and H···H contacts, which are hard to identify and are requisite for crystal packing, can be distinctly observed [16a, 33]. The Hirshfeld surface is defined by $w(r) = 0.5$, where the weight function $w(r)$ is given by the following equation,

$$w(r) = \frac{\sum_{i \in \text{molecule}} \rho_i(r)}{\sum_{i \in \text{crystal}} \rho_i(r)}$$

The weight function represents the ratio of the sum of spherical atom electron densities for a molecule to a similar sum for the entire crystal.^[16a] Several properties of HS can be envisioned and cyphered, in particular, d_e and d_i , which represent the distance from a point on the HS to the nearest nucleus outside or inside, respectively.

The d_{norm} is the normalized contact distance and is defined by taking into account d_e and d_i and the van der Waals radii of the atoms as below:

$$d_{norm} = \frac{d_i r_i^{vdW}}{r_i^{vdW}} + \frac{d_e - r_e^{vdW}}{r_i^{vdW}}$$

Mapping d_{norm} on the HS gives a clear-cut and detailed picture of the interactions happening between adjacent molecules that are shorter than the van der Waals radii sum (visualized as red spots on the HS).

The HSs of **H₂L**, **2** and **3**, are illustrated in Figure S5, showing surfaces that have been mapped with d_{norm} , shape index and curvedness. For a given crystal structure, the HS is unique and suggests the possibility of obtaining additional acumen into the crystal.^[34] The measureable like area, asphericity, globularity and volume can also be calculated using HSs. The term, globularity^[35] is found to be less than unity for **H₂L**, **2** and **3** which indicate that the molecular surface is more structured but not a sphere. The asphericity^[36] is a measure of anisotropy which decreases in the ensuing order for the compounds: **H₂L** > **3** > **2**.

In **H₂L** and **3**, the DHA ring contributes more towards C···H interaction seen as a moderate intense red spot in the HS compared to that of **2** which is observed as light red spot (Figure S5a). Further, the HSs of **H₂L** and **3** show intense red spot on the d_e surface near the phenyl ring which is due to close (ph)C···H(ph) contacts, while in case of **2** is due to close (ph/DHA)C···H(ph). In addition to this, O–H···Cl and C–H···Cl contacts are also seen as intense red spots in **3**. The crystal packing of **3** is mainly controlled by dominant interactions between pyrone –OH and chloride atom observed as strong red spot. Shape index and curvedness can also be used to identify the characteristic packing modes and the ways in which the nearby molecules contact one another. The shape index of **H₂L**, **2** and **3** shows a red concave region on the surface around the acceptor atom and a blue region around the donor H-atom.^[37] Curvedness is a function of the root mean square curvature of the surface and the maps of curvedness on the HSs for **H₂L**, **2** and **3** show no flat surface patches which indicate that there is no stacking interaction between the molecules (Figure 8c).^[37] A major contribution to HSs of **H₂L**, **2** and **3** comes from three kinds of contacts, i.e., C···H, O···H and H···H. The fingerprint plots of **H₂L**, **2** and **3** features spike of various lengths and thickness, and the most prominent being the presence of wing-like peripheral spikes for C···H contact at the top left and bottom right of each plot. The spike at the top left correspond to the points on the surface around the C–H donor, while those at the bottom right correspond to the surface around the π acceptor and a

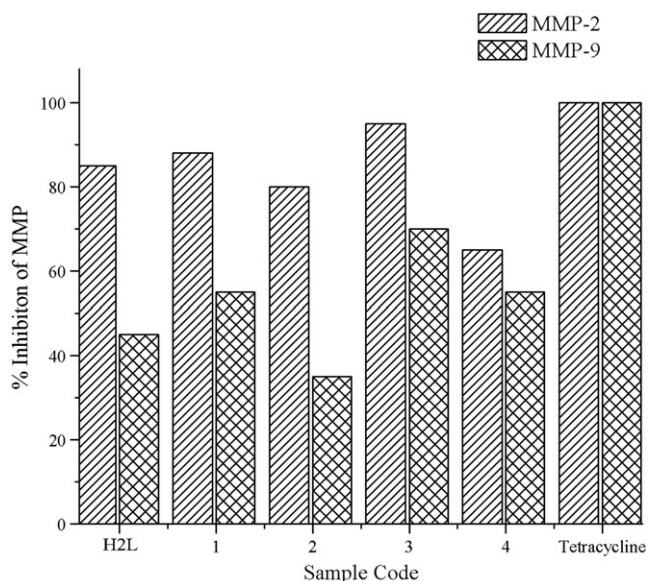


FIGURE 8 Graphical representation of % inhibition of all the test compounds against MMP-9 and MMP-2

similar feature for C \cdots H contact is also observed in FPs of small organic molecules.^[34] In case of **H₂L**, 19.1% of intermolecular contacts are associated with C \cdots H whereas in **2** and **3** it is of 19.2% and 15.0% of the HSs. The non-directional H \cdots H contacts are characterized by broader spikes in **H₂L** and its Ni(II) complex and relatively sharper spikes in the Cu(II) complex [41.0%, 36.8% and 39.3% in **H₂L**, **2** and **3**, respectively]. And, the percentage contribution of H \cdots H contact is also a measure of the strength of the crystal lattice.^[38] The longer and thinner spikes reflect the O \cdots H contacts (19–28%) of the hydrogen bonds present in **H₂L**, **2** and **3**. In ligand, 24.3% of contacts are associated with O \cdots H whereas in **2** and **3** it is of 27.9% and 19.6% of the HSs. The C \cdots C and N \cdots H contacts are present only with a little contribution of 4–7% and 1–3%, respectively, for **H₂L**, **2** and **3**. By comparing the brick red and blue region in Figure S5a, it is seen that the relative contribution of C \cdots H and H \cdots H contacts are comparable for **H₂L** and **3**, while the contribution is entirely different for **2**. A visual inspection of FPs for **H₂L** and **3** reveals that the two molecules are distinct from each other and the main difference is the shortening of C \cdots H contact of **3** relative to **H₂L** with a concomitant increase in the H \cdots H contact distance. Overall, the close contacts are dominated by O \cdots H, C \cdots H and H \cdots H interactions.

3.3 | ¹H NMR spectral studies

¹H NMR spectra of **H₂L** (Figure S6) and **4** (Figure S7) are provided as the supporting material. A broad singlet at 15.89 ppm in the spectrum of free ligand, ascribed to -OH proton is absent in **4**, indicating the coordination of

oxygen of OH group (pyrone ring) *via* deprotonation to the Zn(II) ion. Two broad singlets at 11.78 and 11.36 ppm are assigned to protons of N2 and N1, respectively. These signals have shifted to up-field by few ppm, revealing the breakdown of intramolecular hydrogen bonding upon coordination. The signals due to protons of O3, N1 and N2 are D₂O exchangeable. A singlet observed at 5.85 ppm in free ligand ascribed to -C19H corresponds to one proton. A doublet and triplet at 8.33 and 7.29 ppm in free ligand are assigned to -C12H and -C11H, respectively. The aromatic protons resonated as multiplets in the region 7.66–7.55 ppm in the free ligand have suffered a slight downfield shift in **4**. The -C16H₃ and -C21H₃ protons observed as singlets at 2.11 and 2.61 ppm in uncoordinated ligand have shifted to 2.06 and 2.59 ppm, respectively on complexation.

3.4 | Mass spectral (LC-MS and ESI-MS) analysis

The LC mass spectrum of **H₂L** (Figure S8) has shown a molecular ion peak [M+H]⁺ at m/z 406 corresponding to its molecular mass. In the positive mode, ESI-MS (Figure S9) of **3** base peak observed at m/z 545 exactly corresponds to the mass of [M+Na]⁺ species. Loss of one coordinated chloride ligand, generating a mono-positive ion is evident by the peak observed at m/z 485 and followed by the loss of coordinated water molecule is evident from the peak at m/z 467. This assignment is in good agreement with the structure obtained from SC-XRD study for **3**. In the mass spectra of **1** and **2** (Figure S10), peak observed at m/z 868 and 867 respectively, is assigned to [M+H]⁺ ion. The ESI-MS of **4** (Figure S11) has shown a peak at 871, corresponding to the ion [M-H]⁺. Further, the peak at 300 for all complexes, is due to the loss of a benzoyl fragment of the ligand indicating the ease of cleavage of C7–N1 bond. The peaks observed at m/z of 406 in all the complexes corresponds to [M+H]⁺ species of the corresponding ligand.

3.5 | Electronic spectral studies

The electronic spectra of the ligand, as well as complexes, were recorded in DMF solvent. Strong absorption in the range of 265–275 nm exhibited by ligand is ascribed to intra-ligand $\pi \rightarrow \pi^*$ transitions. This band has remained almost unchanged in the complexes. The $n \rightarrow \pi^*$ transition of azomethine functionality is observed between 304 and 391 nm and has suffered hypsochromic shift upon complexation. This is an indication of coordination of imine nitrogen to the metal ions. The d-d transitions observed at 749 and 850 nm for **1** are assignable to ⁴T_{1g}

(F) \rightarrow $^4T_{2g}$ (F) (ν_1), and $^4T_{1g}$ (F) \rightarrow $^4A_{2g}$ (F) (ν_2) transitions, which are in support for an octahedral geometry of the complex.^[39a,b] Complex **2** has shown its lowest energy transition around 935 nm which is assignable to $^3A_{2g}$ (F) \rightarrow $^3T_{2g}$ (F) (ν_1). The other transition observed around 560 nm are consistent with the energy of $^3A_{2g}$ (F) \rightarrow $^1T_{1g}$ (F) (ν_2), indicating an octahedral transition for **2**. The absorption spectrum of **3** has exhibited a d-d electronic band around 659 nm. Absorptions in this region are typical of species with square pyramidal geometry around the Cu (II) ion.^[39c] The $\pi \rightarrow \pi^*$, $n \rightarrow \pi^*$ and d-d transition bands exhibited by the ligand and its complexes are shown in Figures S12 and S13.

3.6 | Thermo gravimetric (TG) analysis

All the complexes were studied for TG and DTG analysis over the temperature range of 25–1000 °C under nitrogen atmosphere. The thermal decomposition pattern of **1** and **3** (Figure S14 & S15) are dealt in detail.

1 has remained thermally stable up to 313 °C, showing the absence of any lattice held water/solvent molecules. The weight loss of about 46.68% (Calc. 46.72%) in the range of 314–326 °C is due to the loss of one of the ligand molecule. This is clearly evidenced in DTG curve in the form of an endothermic peak at 321 °C. The second ligand molecule has decomposed gradually with the increase in temperature.

The initial weight loss of about 3.33% (Calc. 3.34%) in **3** is due to the loss of lattice held water molecule. Further in the temperature range of 120–240 °C, the complex has lost 9.86% (Calc. 9.91%) of its weight due to the combined loss of one chloride and one water molecules coordinated to the metal ion. This process is further supported by exothermic peaks in DTG curve at 234 °C. Above 241 °C, the complex has gradually lost its weight due to the decomposition of ligand moiety. The TG and DTG analytical data of **1** and **3** are in good agreement with the ascribed structures. The temperature ranges, stages of decomposition, decomposition product loss as well as the found and calculated weight-loss percentages of the complexes are summarized in Table S1 support the suggested composition for the complexes.

3.7 | Pharmacological studies

3.7.1 | *In vitro* anti-inflammatory activity

Gelatin zymography is a modest yet strapping technique to detect proteolytic enzymes capable of degrading gelatin from various biological sources. The two gelatinases (MMP-2 and MMP-9) have gelatin-binding domains that resemble an equivalent motif in fibronectin. This motif

is involved in the binding of fibronectin to denatured collagen, and in MMP-2 and MMP-9, it probably augments the interaction with gelatin/gelatin-like substrates.^[40] It is markedly useful for the assessment of two vital members of the matrix metalloproteinase family, such as 72 kDa gelatinase A (MMP-2) and 92 kDa gelatinase B (MMP-9), which have herculean gelatin-degrading properties.^[41] Gelatinases present in the physiological system, play an essential role in inflammation and autoimmunity conditions.^[42] Activated inflammatory cells and dermal fibroblasts can express numerous proteinases designated as matrix metalloproteinases (MMPs) able to degrade all connective tissue macromolecules. Amongst these gelatinases, e.g., MMP-2 and MMP-9 together with interstitial collagenase have been presumed to be of importance in connective tissue remodeling consecutive to inflammation.^[43] This method is used to detect gelatinase activity, especially MMP-2 and MMP-9. MMP-2 and MMP-9 remain inactive, while they are with their pro-domains and require denaturation to get activated. Then, it could be detected on gelatin zymograms as one or two white bands (pro and active forms) after staining with coomassie blue. The *in vitro* anti-inflammatory activity results are attained from the % bands of MMP-2 and MMP-9 which was detected for each sample screened from the gelatin zymogram by gel electrophoresis techniques. The percentage of inhibition of MMP-2 and MMP-9 for each sample is calculated by subtracting from 100 with the % bands of MMP-2 and MMP-9, respectively. The *in vitro* anti-inflammatory activity results of MMP-2 and MMP-9 are detected as white bands (Figure S16) and the percentage of inhibition of the compounds are tabulated in Table 5. The obtained results revealed that all the compounds were active against MMP-2. Similarly, the compounds **H₂L**, **1** and **3** were active against MMP-9, whereas **2** and **4** showed slight inhibitory activity against MMP-9. The results are also represented as bar diagram in Figure 8.

TABLE 5 *In vitro* anti-inflammatory results of **H₂L** and its complexes with % bands and % inhibition of MMP-2 and MMP-9

Sample Code	% Bands of MMP		% Inhibiton of MMP	
	MMP-2	MMP-9	MMP-2	MMP-9
H₂L	15	55	85	45
1	12	45	88	55
2	20	65	80	35
3	05	30	95	70
4	35	45	65	55
Tetracycline	00	00	100	100
DMSO Control	-	-	-	-

3.7.2 | *In vitro* anticancer activity at one dose (10^{-5} M concentration)

Two among the five newly synthesized compounds, **H₂L** and **3** were selected and submitted to *in vitro* anticancer screening in a single dose (10^{-5} M concentration) in the full NCI 60 cell panel.^[29–31] Using this data, it is possible to anticipate the mechanism of action of each test compound, or to define that the response pattern is distinctive and not like any of the standard prototype compounds included in NCI database. The single-dose data is graphed as the mean of the percent growth of the treated cells, relative to the no-drug control, and relative to the time zero number of cells. This permits detection of both growth inhibition and cytotoxicity. The output from the single dose screen is available for COMPARE analysis.^[44,45] **H₂L** and **3** have been evaluated by NCI, on all the 60 human cancer cell lines organized into subpanels derived from nine different human cancer types: leukemia, melanoma, lung, colon, renal, ovarian, breast, prostate and CNS, at one dose (10^{-5} M concentration) primary anticancer assay (Table 6).

The most sensitive cell lines for **H₂L** are Leukemia CCRF-CEM (GI% 24.58), CNS Cancer SF-268 (GI % 24.72), Melanoma UACC-257 (GI % 30.20), Ovarian Cancer OVCAR-4 (GI% 53.08 or GP% 46.92) and SK-MEL-5 (GI % 74.63 or GP% 25.37), Breast Cancer MDA-MB-468 (GI % 23.30), Breast Cancer MDA-MB-231/ATCC (GI % 22.89) and Breast Cancer T-47D (GI % 20.97) and for **3** are Leukemia K-562 (GI% 30.26), Ovarian Cancer SK-OV-3 (GI% 30.85) and Breast Cancer MCF7 (GI% 19.76) (Table 6). Despite the average activity of **3** being less than that of **H₂L**, **3** outperformed **H₂L** against several cell lines, namely K-562 (Leukemia), EK VX (Non-Small Cell Lung Cancer), HT29 (Colon Cancer), SNB-75 (CNS Cancer), SK-OV-3 (Ovarian Cancer), MCF7 (Breast Cancer) (Table 6). The tested compounds show a different strength of anticancer activity, **H₂L** has moderate anticancer activity, but **3** possess a significant influence on several cancer cell lines. This activity pattern is likely due to distinctive molecular mechanisms of action for the tested compounds.

3.7.3 | DNA cleavage studies

The interactions between the free ligand and its complexes ($100 \mu\text{g L}^{-1}$) with DNA were analyzed with the aid of agarose gel electrophoresis method. The photograph depicted in Figure 9 show bands with different bandwidths compared to the marker and control, and this is the differentiating criterion for cleavage abilities of the compounds with CT-DNA in this study. Control

TABLE 6 Growth inhibition (GI %) in single dose assay (10^{-5} M concentration) for compound **H₂L** (NSC: D-797749/1) and **3** (NSC: D-797758/1)

Panel/Cell line	Growth Inhibition (GI %)	
	H₂L	3
Leukemia		
CCRF-CEM	24.58	08.19
K-562	17.11	33.26
MOLT-4	11.87	10.67
Non-Small Cell Lung Cancer		
A549/ATCC	16.94	03.85
EK VX	16.73	18.64
HOP-62	14.56	06.17
NCI-H23	11.02	10.97
NCI-H522	15.97	15.75
Colon Cancer		
HT29	01.58	16.67
CNS Cancer		
SF-268	24.72	06.27
SNB-75	06.45	14.24
Ovarian Cancer		
OVCAR-3	19.29	01.94
SK-OV-3	04.44	30.85
Breast Cancer		
MCF7	19.56	19.76
T-47D	20.97	19.95

experiment suggests that untreated DNA did not show any notable DNA cleavage, even after a long exposure time (lane A). Further, when the genomic DNA is allowed to interact with **H₂L** and its complexes, a substantial decrease in the intensities of the bands for the ligand and its complex bound DNA as compared to the untreated control DNA is observed, in case of **H₂L**, **1**, **2** and **3** (lanes C, D, E and F), shows a significant decrease in intensity and bandwidth, indicating the sufficient cleavage of CT-DNA. Whereas, **4** (lane G) has shown a slight decrease in the intensity and bandwidth compared to the control due to moderate cleavage of CT-DNA. These results suggest that **H₂L** and its complexes can cleave CT-DNA to different degrees. We conclude that **1** exhibits greater cleavage potential.

3.8 | Docking Study

Molecular docking studies are undertaken to envisage the interaction between the synthesized prodrugs and a protein, which would enlighten the behavior of the

(a) (b) (c) (d) (e) (f) (g)

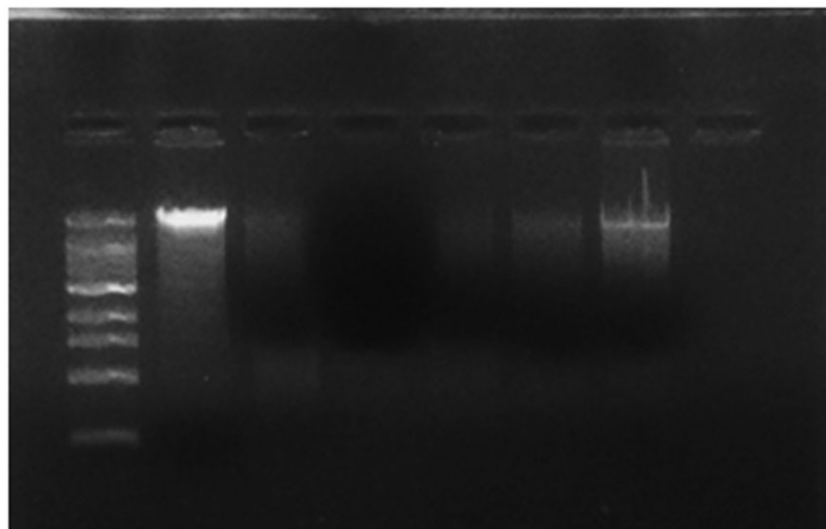


FIGURE 9 Photograph of gel electrophoresis experiment of H_2L series on Calf-thymus DNA. Lane A, DNA marker; lane B, untreated DNA; lane C, H_2L ; lane D, 1; lane E, 3; lane F, 2; lane G, 4

former in the binding site of target proteins to elucidate the regulation of homologous biochemical processes. The study aims to achieve an optimized conformation for both the protein and drug with relative orientation between them such that the free energy of the overall system was minimized. The primary aim of the docking was to identify the preferred binding mode of H_2L and its complexes with the COX-2 enzyme. The calculations were performed on Autodock Vina using the X-ray crystal structure of celecoxib bound at the COX-2 active sites (PDB code: 3LN1) as protein model.

Molecular surface visualization and crystallographic studies revealed that the COX-2 active site consists of mostly hydrophobic residues. There are three main pockets (S1, S2, S3) and one shallow pocket (S4) in COX-2 active site, wherein, Pocket S1 consists of the amino acid residues His90, Ala516, Arg513, Gln192 and the backbone of Phe518, whereas Pocket S2 is localized at the top of the channel and comprises of several hydrophobic amino acid residues Met522, Tyr348, Tyr385, Trp387 and Phe518. Pocket S3 confined in the mouth of the active site and is delimited by

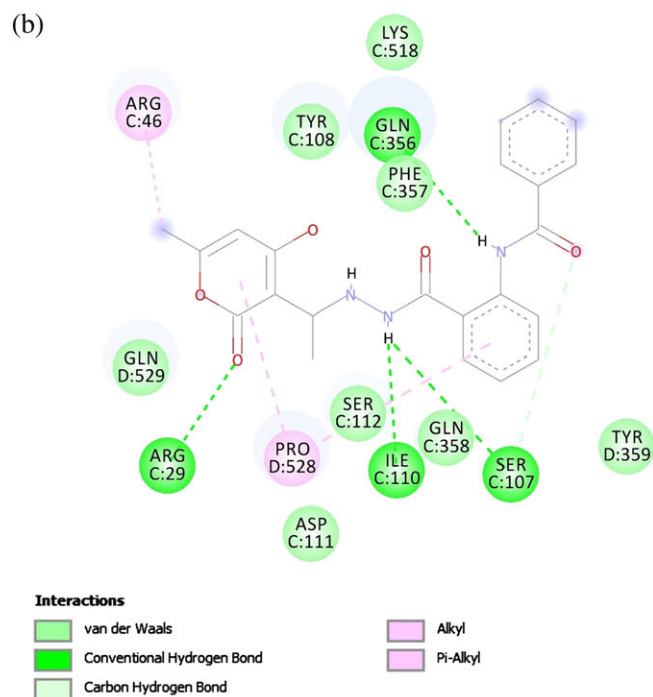
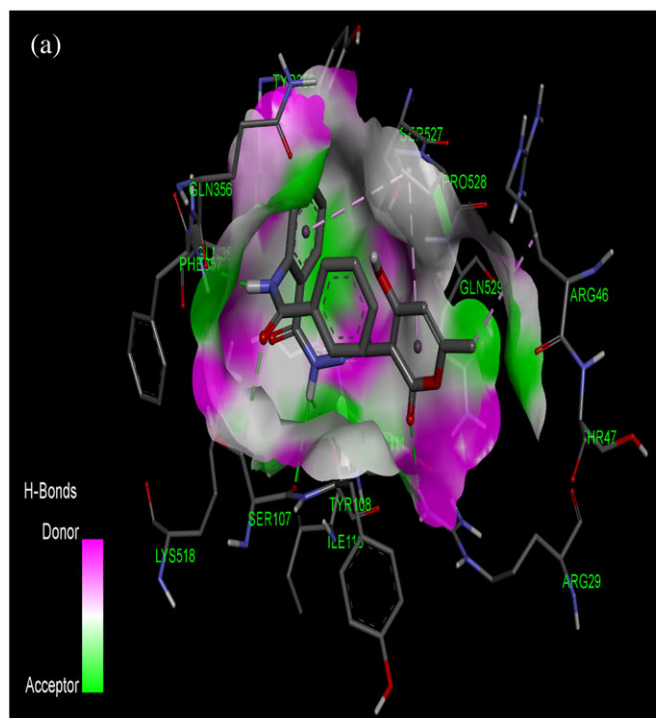


FIGURE 10 (a) Docking conformation of H_2L with amino acid residues at the active site of the enzyme. (b) 2D plot displaying various types of molecular interactions of H_2L with enzyme residues

Tyr355, Leu359, Val116 and Arg120. Shallow pocket S4 is localized in a hydrophobic area close to the hydrophobic pocket S2 which has a lesser number of residues, including Ile345, Leu534 and Leu531 [46]. The inhibitors (**H₂L** and its complexes) were docked at the active site of COX-2 and various interactions have been laid out (Figure 10–12). The most prominent interactions were observed for **1** with the lowest binding energy of -12 kcal/mol amongst all other compounds tested with the protein (Table 7). The secondary amidic NH of **4** is in H-bonding with the oxygen of carbonyl group of Arg46 with a distance of 2.39 Å. The Arg46, in addition, forms an alkyl and π -alkyl interactions with phenyl ring and methyl protons

of hydrazone. In case of **1** and **2**, the Gln356 exerts dual H-bonding tendency towards NH of hydrazone ($>N-H\cdots O=C<$, 2.39 Å) and amidic proton ($>N-H\cdots O=C<$, 2.52 Å). The other non-coordinating amide NH is in H-bond bonding with Tyr108 which in turn is in π - π interaction in T-shape. Whereas for **3** oxygen of coordinated water molecule makes a short distance H-bonding with indole NH proton of Trp309 ($>N-H\cdots O=C<$, 1.85 Å). Adjacent to this is the Ser34 in a conventional H-bonding distance of 2.68 Å with metal coordinated oxygen of pyrone ring. The carbonyl oxygen of Gly121 makes double H-bond interactions with NH of hydrazone and amide with bond distances of 2.63 and 2.51 Å, respectively.

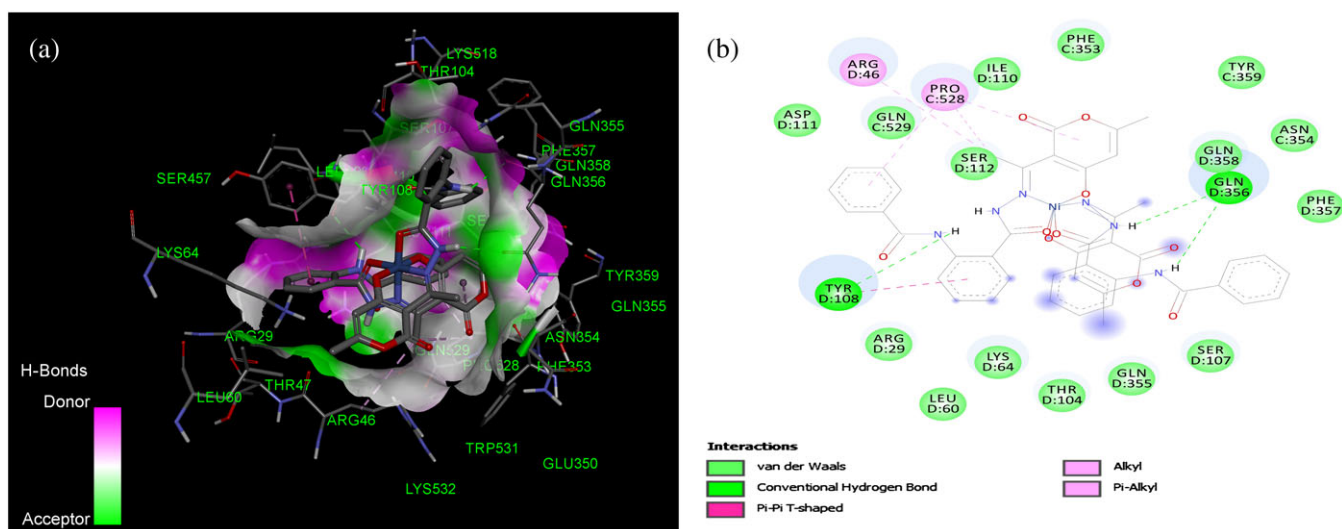


FIGURE 11 (a) Docking conformation of **2** with amino acid residues at the active site of the enzyme. (b) 2D plot displaying various types of molecular interactions of **2** with enzyme residues

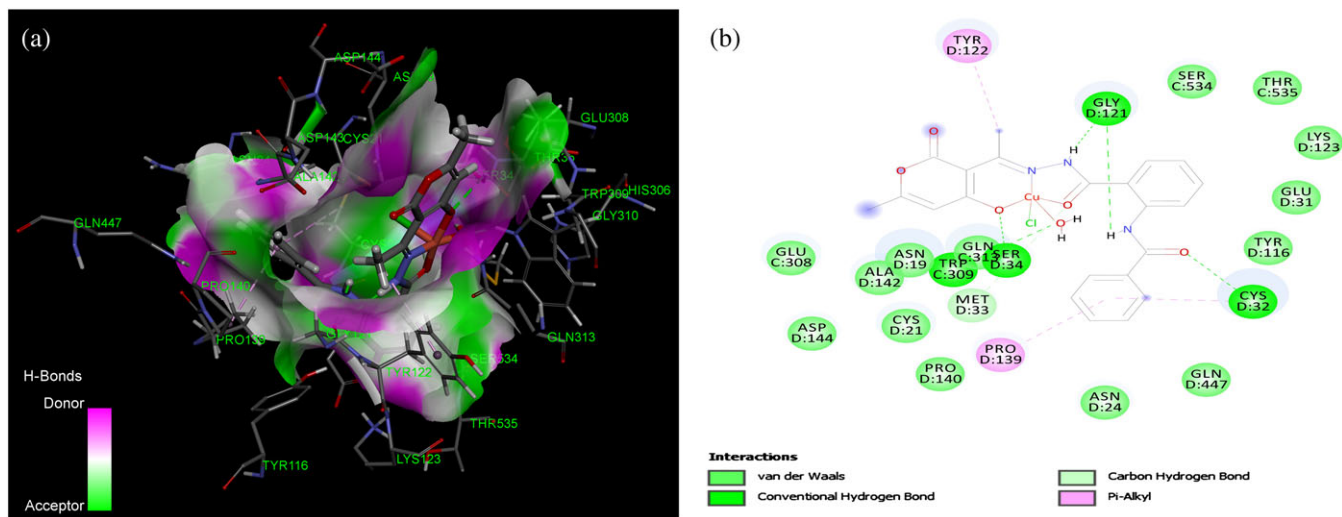


FIGURE 12 (a) Docking conformation of **3** with amino acid residues at the active site of the enzyme. (b) 2D plot displaying various types of molecular interactions of **3** with enzyme residues

TABLE 7 Molecular docking results of H₂L and its complexes

Compound	Binding energy (kcal/mol)	PSA* at pH 7.4	No. of hydrogen bonds	Interacting residues	Distance (Å)
H ₂ L	-8.4	117	4	Arg29 Ser107 Ile110 Gln356	2.37 3.07 2.51 2.28
1	-12.0	260	3	Tyr108 Gln356	2.31 2.43, 2.49
2	-11.4	260	3	Tyr108 Gln356	2.62 2.39, 2.52
3	-11.2	155	5	Ser34 Cys32 Gly121 Trp309	2.68 2.23 2.51, 2.63 1.85
4	-11.5	260	2	Arg46 Gln356	2.37 2.59

*PSA= Polar surface area

4 | CONCLUSIONS

In the present work, we synthesized and characterized a new tridentate ligand, H₂L and its complexes in good yields. Analytical and spectroscopic data for the complexes indicate a 1:1 (M:L) stoichiometry for **3** adopting a square-pyramidal and 1:2 for **1**, **2** and **4** adopting an octahedral geometry around the metal ion. The organic motif, H₂L has coordinated through an amide carbonyl oxygen (O2), azomethine nitrogen (N3) and pyrone carbonyl oxygen (O3H) *via* deprotonation in case of all the complexes. Thus, H₂L acts as a monobasic tridentate ligand. The tentative structures for metal complexes are depicted in Scheme 2. All interactions in crystal structures of H₂L, **2** and **3** have studied by Hirshfeld surface analysis. H₂L and its complexes have screened for their *in vitro* anti-inflammatory activity. The results showed that activity of H₂L has improved on complexation is probably due to the greater lipophilic nature of the complexes.^[47a-e] Among the complexes, **3** has shown highest activity. The difference in activity among the tested compounds may be attributed to the electrostatic nature of ligand and central metal ion. Among the 60 human cancer cell lines tested, both H₂L and **3** have moderately inhibited the growth of K-562 (Leukemia), EKVX (Non-Small Cell Lung Cancer), SNB-75 (CNS Cancer), SK-OV-3 (Ovarian Cancer), MCF7 (Breast Cancer). Further, the H₂L and its complexes were also tested for their potential CT-DNA cleavage activity. The molecular modelling study of all the compounds with inhibitor bound COX-2 revealed that the molecules fit in the active site of the receptor.

ACKNOWLEDGMENTS

Authors thank USIC, Karnatak University, Dharwad for IR, UV, TG/DTG analysis and Waters company for ESI mass analysis. NCI-USA is acknowledged for NCI-60 Human Tumor Cell Lines Screen under Developmental Therapeutics Program. Recording of ¹H NMR spectra from IISC-Bangalore is greatly acknowledged. One of the authors, Umashri also thank Niranjana Acharya of Sequent Scientific Limited for his generous help in mass analysis. One of the authors, Geeta H. Chimmalagi acknowledges UGC for providing RFSMS scholarship. We acknowledge DST and UGC New Delhi, India, for the financial support through UPE-FAR-I and DST-PURSE Phase II programmes.

ORCID

Kalagouda B. Gudasi  <http://orcid.org/0000-0002-0063-7656>

REFERENCES

- [1] B. Desoize, *Crit. Rev. Oncol. Hematol.* **2002**, *42*, 213.
- [2] a) M. Mohamadi, S. Y. Ebrahimipour, J. Castro, M. Torkzadeh-Mahani, *J. Photochem. Photobiol. B* **2016**, *158*, 219; b) M. Mohamadi, S. Y. Ebrahimipour, M. Torkzadeh-Mahani, S. Foro, A. Akbari, *RSC Adv.* **2015**, *122*, 101063.
- [3] a) S. Y. Ebrahimipour, I. Sheikhshoae, J. Castro, M. Dušek, Z. Tohidiana, V. Eigner, M. Khaleghi, *RSC Adv.* **2015**, (115), 95104; b) S. Y. Ebrahimipour, M. Mohamadi, M. T. Mahani, J. Simpson, J. T. Mague, I. Sheikhshoae, *Eur. J. Med. Chem.* **2017**, *140*, 172; c) I. Sheikhshoae, S. Y. Ebrahimipour, N. Lotfi, J. T. Mague, M. Khaleghi, *Inorganica Chim. Acta* **2016**, *442*, 151;

- d) R. Takjoo, A. Akbari, S. Y. Ebrahimipour, M. Kubicki, M. Mohamadi, N. Mollania, *Inorganica Chim. Acta* **2017**, 455, 173; e) S. Y. Ebrahimipour, M. Mohamadi, I. Sheikhshoae, S. Suárez, R. Baggio, M. Khaleghi, *Res. Chem. Intermed.* **2016**, 42, 611.
- [4] N. Bharti, M. R. Maurya, F. Naqvi, A. Bhattacharya, S. Bhattacharya, A. Azam, *Eur. J. Med. Chem.* **2000**, 35, 481.
- [5] a) P. Krishnamoorthy, P. Sathyadevi, A. H. Cowley, R. R. Butorac, N. Dharmaraj, *Eur. J. Med. Chem.* **2011**, 46, 3376; b) P. Krishnamoorthy, P. Sathyadevi, R. R. Butorac, A. H. Cowley, N. S. P. Bhuvanesh, N. Dharmaraj, *Dalton Trans.* **2012**, 41, 4423.
- [6] a) S. Y. Ebrahimipour, I. Sheikhshoae, J. Simpson, H. Ebrahimnejad, M. Dusek, N. Kharazmia, V. Eigner, *New J. Chem.* **2016**, 40, 2401; b) F. Heidari, S. J. A. Fatemi, S. Y. Ebrahimipour, H. Ebrahimnejad, J. Castro, M. Dušek, V. Eigner, *Inorg. Chem. Commun.* **2017**, 76, 1; c) M. Mohamadi, E. Faghih-Mirzaei, S. Y. Ebrahimipour, I. Sheikhshoae, W. Haase, S. Foro, *J. Mol. Struct.* **2017**, 1139, 418.
- [7] A. A. Napoleon, F.-R. N. Khan, *Med. Chem. Res.* **2014**, 23, 4749.
- [8] B. Rosenberg, L. Vancamp, *Nature* **1969**, 222, 385.
- [9] D. Denoyer, S. Masaldan, S. La Fontaineab, M. A. Cater, *Metallomics* **2015**, 7, 1459.
- [10] (a) A. I. Vogel, *Vogel's Textbook of Practicle Organic Chemistry*, 4th ed., ELBS, London **1978**; (b) L. Wilfred, E. Armarego, C. L. Lin Chai, *Purification of Laboratory Chemicals*, 5th ed., Butterworth-Heinemann, Elsevier Science, Bodmin, Cornwall, UK **2003**.
- [11] A. Kalusa, N. Chessum, K. Jones, *Tetrahedron Lett.* **2008**, 49, 5840.
- [12] N. P. Peet, *Synthesis* **1984**, 12, 1065.
- [13] G. M. Sheldrick, SHELXTL. Version 5.0, Bruker AXS Inc., Madison, WI, **2001**.
- [14] S. K. Wolff, D. J. Grimwood, J. J. McKinnon, M. J. Turner, D. Jayatilaka, M. A. Spackman, *CrystalExplorer 3.1*, University of Western Australia, Crawley, **2012**.
- [15] F. L. Hirshfeld, *Theor. Chim. Acta* **1977**, 44, 129.
- [16] (a) M. A. Spackman, D. Jayatilaka, *CrystEngComm* **2009**, 11, 19; (b) A. Massoud, V. Langer, Y. M. Gohar, M. A. M. Abu-Youssef, J. Jänis, G. Lindberg, K. Hansson, L. Öhrström, *Inorg. Chem.* **2013**, 52, 4046.
- [17] N. S. Naik, L. A. Shastri, S. D. Joshi, S. R. Dixit, B. M. Chougala, S. Samundeeswari, M. Holiyachi, F. Shaikh, J. Madar, R. Kulkarni, V. Sunagar, *Bioorganic Med. Chem.* **2017**, 25, 1413.
- [18] a) M. C. Alley, D. A. Scudiero, A. Monks, M. L. Hursey, M. J. Czerwinski, D. L. Fine, B. J. Abbott, J. G. Mayo, R. H. Shoemaker, M. R. Boyd, *Cancer Res.* **1988**, 48, 589; b) M. R. Boyd, K. D. Paull, *Drug Dev. Res.* **1995**, 34, 91; c) M. R. Grever, S. A. Schepartz, B. A. Chabner, *Semin Oncol.* **1992**, 19, 622.
- [19] J. Sambrook, E. F. Fritsch, T. Maniatis, *Molecular Cloning. A Laboratory Manuals*, 4th ed., Cold Spring Harbor Laboratory Press, New York **1989**.
- [20] J. L. Wang, D. Limburg, M. J. Graneto, J. Springer, J. R. Hamper, S. Liao, J. L. Pawlitz, R. G. Kurumbail, T. Maziasz, J. J. Talley, J. R. Kiefer, J. Carter, *Bioorg. Med. Chem. Lett.* **2010**, 20, 7159.
- [21] O. Trott, A. J. Olson, *J. Comput. Chem.* **2010**, 31, 455.
- [22] F. Neese, *Wiley Interdiscip Rev Comput Mol Sci.* **2012**, 2, 73.
- [23] A. Schäfer, C. Huber, R. Ahlrichs, *J. C. Phys.* **1994**, 100, 5829.
- [24] M. D. Hanwell, D. E. Curtis, D. C. Lonie, T. Vandermeersch, E. Zurek, G. R. Hutchison, *Aust. J. Chem.* **2012**, 4, 1.
- [25] E. F. Pettersen, T. D. Goddard, C. C. Huang, G. S. Couch, D. M. Greenblatt, E. C. Meng, T. E. Ferrin, *J. Comput. Chem.* **2004**, 25, 1605.
- [26] M. F. Sanner, *J. Mol. Graphics Modell.* **1999**, 17, 57.
- [27] A. Djedouani, A. Bendaas, S. Boufas, M. Allain, G. Bouetd, M. Khand, *Acta Cryst. E* **2007**, 63, 1271.
- [28] R. Shakya, C. Imbert, H. P. Hratchian, M. Lanznaster, M. J. Heeg, B. R. McGarvey, M. Allard, H. B. Schlegel, C. N. Verani, *Dalton Trans.* **2006**, (21), 2517.
- [29] (a) K. K. Narang, U. S. Yadav, *Ind. J. Chem.* **1979**, 19A, 697. (b) K. K. Narang, U. S. Yadav, *Ind. J. Chem.* **1981**, 20A, 404.
- [30] A. W. Addison, T. N. Rao, J. Reedijk, J. van Rijn, G. C. Verschoor, *Dalton Trans.* **1984**, 0, 1349.
- [31] J. R. Dilworth, J. Hyde, P. Lyford, P. Vella, K. Venkatasubramaman, J. A. Zubieta, *Inorg. Chem.* **1979**, 18, 268.
- [32] D. Patra, N. Biswas, B. Kumari, P. Das, N. Sepay, S. Chatterjee, M. G. B. Drewe, T. Ghosh, *RSC Adv.* **2015**, 5 92456.
- [33] H. F. Clausen, M. S. Chevallier, M. A. Spackman, B. B. Iversen, *New J. Chem.* **2010**, 34, 193.
- [34] S. Y. Ebrahimipoura, B. Machura, M. Mohamadi, M. Khaleghi, *Microb. Pathog.* **2017**, 113, 160.
- [35] A. Y. Meyer, *Chem. Soc. Rev.* **1986**, 15, 449.
- [36] A. Baumgärtner, *J. Chem. Phys.* **1993**, 99, 7496.
- [37] S. K. Seth, D. Sarkar, A. Roy, T. Kar, *CrystEngComm* **2011**, 13, 6728.
- [38] S. Grabowsky, P. M. Dean, B. W. Skelton, A. N. Sobolev, M. A. Spackman, A. H. White, *CrystEngComm* **2012**, 14, 1083.
- [39] (a) U. Kendur, G. H. Chimmalagi, S. M. Patil, K. B. Gudasi, C. S. Frampton, C. V. Mangannavar, I. S. Muchchandi, *J. Mol. Struct.* **2018**, 1153, 299; (b) N. Sathyanarayana, *Electronic Absorption Spectroscopy and Related Techniques*, 1st ed., University Press **2001**; (c) A. B. P. Lever, *Inorganic Electronic Spectroscopy*, 2nd ed., Elsevier, Amsterdam, Netherlands **1984**.
- [40] W. C. Parks, C. L. Wilson, Y. S. López-Boado, *Nat. Rev. Immunol.* **2004**, 4, 617.
- [41] S. Loffek, O. Schilling, C. W. Franzke, *Eur Respir J.* **2011**, 38, 191.
- [42] U. Galm, S. Heller, S. Shapiro, M. Page, L. H. Shu-Ming Li, *Antimicrob. Agents Chemother.* **2004**, 48, 1307.
- [43] S. Sakamoto, M. Sakamoto, *Mol. Aspects Med.* **1988**, 10, 299.
- [44] K. D. Paull, R. H. Shoemaker, L. Hodes, A. Monks, D. A. Scudiero, L. Rubinstein, J. Plowman, M. R. Boyd, *J. Natl. Cancer Inst.* **1989**, 81, 1088.
- [45] D. W. Zaharevitz, S. L. Holbeck, C. Bowerman, P. A. Svetlik, *J. Mol. Graphics Modell.* **2002**, 20, 297.
- [46] S. Bouaziz-Terrachet, A. Toumi-Maouche, B. Maouche, S. Taïri-Kellou, *J. Mol. Model.* **2010**, 16, 1919.

- [47] (a) S. Chung-Hang Leung, H.-J. Z. Lin, D.-L. Ma, *Chem. Sci.* **2015**, *6*, 871; (b) R. S. Hoonur, B. R. Patil, D. S. Badiger, R. S. Vadavi, K. B. Gudasi, P. R. Dandawate, M. M. Ghaisas, S. B. Padhye, M. Nethaji, *Eur. J. Med. Chem.* **2010**, *45*, 2277; (c) B. G. Tweedy, *Phytopathology.* **1964**, *55*, 910; (d) T. D. Thangadurai, K. Natarajan, *Transition Met. Chem.* **2001**, *26*, 500; (e) J. Joseph, K. Nagashri, G. A. B. Rani, *J. Saudi Chem. Soc.* **2013**, *17*, 285.

SUPPORTING INFORMATION

Additional Supporting Information may be found online in the supporting information tab for this article.

How to cite this article: Kendur U, Chimmalagi GH, Patil SM, Gudasi KB, Frampton CS. Synthesis, structural characterization and biological evaluation of mononuclear transition metal complexes of zwitterionic dehydroacetic acid *N*-aroylhydrazone ligand. *Appl Organometal Chem.* 2018;e4278. <https://doi.org/10.1002/aoc.4278>